A Dual-SSHC Rectifier With Digital-DCB MPPT for Triboelectric Energy Harvesting

Peng, Wenyu; Yue, Xinling; Van Driel, Willem D.; Zhang, Guoqi; Du, Sijun

DOI
10.1109/OJSSCS.2025.3573905

Publication date
2025

Document Version
Final published version

Published in
IEEE Open Journal of the Solid-State Circuits Society

IEEE Open Journal of the
Solid-State Circuits Society

Received 11 February 2025; revised 27 April 2025; accepted 16 May 2025. Date of publication 27 May 2025; date of current version 3 July 2025.

Digital Object Identifier 10.1109/OJSSCS.2025.3573905

A Dual-SSHC Rectifier With Digital-DCB MPPT for Triboelectric Energy Harvesting

WENYU PENG (Student Member, IEEE), XINLING YUE (Student Member, IEEE), WILLEM D. VAN DRIEL, GUOQI ZHANG (Fellow, IEEE), AND SIJUN DU (Senior Member, IEEE)

Department of Microelectronics, Delft University of Technology, 2628 CD Delft, The Netherlands

CORRESPONDING AUTHOR: S. DU (e-mail: sijun.du@tudelft.nl)

ABSTRACT Triboelectric nanogenerator (TENG), advantageous in high energy density and flexibility, is promising as a sustainable energy source but can hardly be used to power edge devices directly due to its high-voltage ac output and varying capacitive impedance. To address it, this work proposes a power-conditioning interface with a fully integrated dual synchronous switch harvesting on capacitors (D-SSHC) rectifier for triboelectric energy extraction. Furthermore, a full digital duty-cycle-based (DCB) maximum power point tracking (MPPT) algorithm is developed to optimize the energy harvesting efficiency with simple implementation and continuous tracking. Designed and fabricated in a 0.18-μm BCD process, the proposed interface can extract energy at a maximum output voltage of 70 V. According to the measurement results, it achieves 99% MPPT efficiency and an energy extraction improvement of 598% compared to a full-bridge rectifier.

INDEX TERMS Energy harvesting, maximum power point tracking (MPPT), power management, rectifier, switched-capacitor converter, synchronous switching, triboelectric nanogenerator (TENG).

I. INTRODUCTION

EDGE computing and Internet of Things (IoT) technologies have rapidly advanced in recent years, enhancing convenience in daily life. However, the widespread use of electronic devices, primarily powered by batteries, raises concerns about environmental pollution and limits device lifespan. Unlike batteries, energy harvesting technologies can continuously obtain energy from the environment, making them a more sustainable and eco-friendly alternative. Mechanical energy harvesting is one of the most popular approaches due to its accessibility and robustness in many applications, and the method of converting and managing mechanical energy efficiently has gained much research interest. In the past decade, a novel method to convert mechanical energy to electrical energy was proposed, the triboelectric nanogenerator (TENG) [1]. It shows improved compatibility and high energy density and thus is suitable for mechanical energy harvesting in variable scenarios, e.g., human movement, moving vehicles, and water wave [2], [3], [4], [5]. However, managing triboelectric energy is challenging. The model of a typical TENG is composed of an alternating current source (I_T) and a small varying capacitor (C_T) connected in parallel. Due to the small C_T, the static charge induces high ac voltage amplitude, which can hardly be utilized directly by electronic devices.

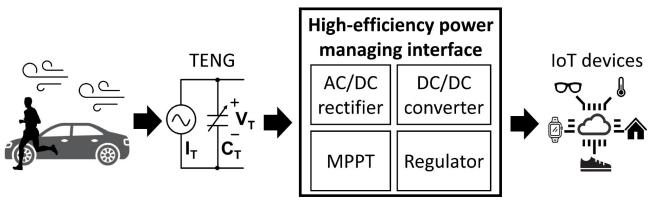

FIGURE 1. TEH system to power IoT devices.

To utilize the triboelectric energy, a power-conditioning interface is needed to manage the input power and convert it to a low-voltage dc output, of which the typical structure is shown in Fig. 1. In prior works, several dedicated rectifiers were proposed and applied for triboelectric energy harvesting (TEH) [6], [7]. To tackle the asymmetric output of a TENG caused by the varying C_T, a dual-output rectifier (DOR) was proposed with two output capacitors [8], [9], [10], [11]; however, this bridge-configured passive rectifier sets threshold for energy extraction related to the output voltage and energy will only be rectified when the input voltage is higher than the output. Consequently, when the input

voltage is lower than the output, energy cannot be extracted by the interface but is wasted in charging/discharging the internal capacitor of the TENG. In comparison, a half-bridge rectifier [12] and Bennet's doubler [13], [14] discard the energy in the negative-V_T semi-period to achieve better energy extraction performance in the positive-V_T semi-period, which still introduces energy wastage.

A better way to extract energy from TENGs is to use active interfaces employing bias-flip or synchronous electrical charge extraction (SECE) techniques. The inductor-based bias-flip technique, i.e., synchronized switch harvesting on inductor (SSHI), was first proposed for piezoelectric energy harvesting [15], and has been demonstrated effective in TEH in [16] and [17]. It flips the voltage across the inherent capacitor when I_T crosses zero so that the output voltage can reach the threshold voltage with little charge waste. Regarding the SECE technique, the full-bridge rectifier (FBR) is directly connected to a buck-boost dc–dc converter. The source is opened until the voltage on C_T reaches extrema, and then the dc–dc converter extracts all the charge from C_T. Due to the high open-circuit voltage amplitude of TENG (V_{OC}), a multishot SECE interface was proposed to extract triboelectric energy in small pieces to restrict the input voltage within the technical tolerance [18]. In comparison, the bias-flip technique has better output performance than the SECE interface since the flipped voltage forms extra load to the TENG so that additional mechanical energy can be harvested, resulting in higher electrical energy output. Nevertheless, both SSHI and SECE utilize inductors. Due to the high voltage on the TENGs, inductors with high-quality factors are required for high efficiency, resulting in bulky TEH systems. On the other hand, the capacitor-based bias-flip technique, i.e., synchronized switch harvesting on capacitors (SSHC), was proposed for the piezoelectric energy harvesting [19], [20], [21], [22], [23]. It is integrable with on-chip capacitors, achieving improved robustness and long-term reliability by reducing the risk of mechanical failure and loose connections; however, directly using it in TEH will result in poor performance due to the time-varying C_T. Another recently proposed switched-capacitor-based TEH interface is the electrostatic charge boosting (ECB) rectifier [24], [25]. It achieves better performance than the bias-flip technique in TENG with varying C_T; however, it relies on a high C_T variation ratio and a relatively low V_{OC}, limiting its applications.

Though the bias-flip rectifier provides promising performance among other active circuits, its output power is not always the maximum as it is affected by the extracting voltage. Therefore, locating the maximum power point (MPP) and maintaining the extracting voltage at this MPP is necessary to ensure the greatest extraction performance. The conventional methods to achieve MPP tracking (MPPT) consist of perturb and observe (P&O) [26] and fractional open-circuit voltage (FOCV) [27]. The P&O technique is advantageous in accurate tracking but is power-hungry and complicated to implement. The FOCV method utilizes

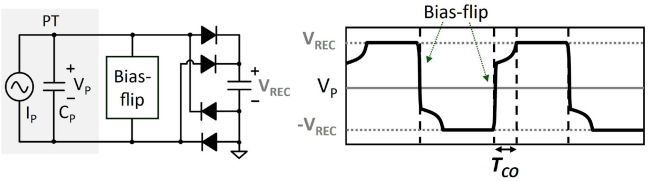

FIGURE 2. Bias-flip rectifier and the associated waveform for piezoelectric energy harvesting.

the mathematic relationship between V_{OC} and the voltage corresponding to the MPP, V_{MPP}, to maximize the power output. It needs to sample the V_{OC} of the TENG, which is too high to be directly sampled and results in a waste of energy during the sampling period and low MPPT efficiency when V_{OC} is fast-varying. Another MPPT technique proposed recently is the duty-cycle-based MPPT (DCB-MPPT) [28]. It reveals the relationship between the conducting duty cycle of the rectifier and the output power. In piezoelectric energy harvesting, the MPP is reached when the conduction duty cycle of the rectifier is 50%. Utilizing this method in TEH is attractive due to its simple implementation and continuous high-accuracy tracking. However, a TENG has a different model from the piezoelectric transducer (PT) so a new DCB algorithm is needed for TEH.

In this work, we propose a fully integrated dual-SSHC (D-SSHC) rectifier with a DCB MPPT technique, designed with a small form factor to facilitate compact packaging and enhance mechanical robustness [20]. The proposed circuits can achieve continuous MPPT for TENGs with time-varying C_T. The following sessions are organized as follows. Section II introduces the fundamentals for the DCB MPPT and the TENG characteristics. Section III presents the theoretical analysis of the DCB MPPT algorithm for TENG. Section IV presents the system implementation, including the top architecture and the details of key blocks. Section V presents and discusses the measurement results. Section VI draws the conclusion.

II. BACKGROUND

A. DCB MPPT FUNDAMENTALS

The DCB MPPT technique was first proposed for piezoelectric energy harvesting, where the PT shares an equivalent electronic model similar to TENG's concerning an ac source in parallel with an inherent capacitor. The difference is that the capacitor of a PT is constant, while that of a TENG can be time-varying. When a bias-flip rectifier is applied to a PT, the waveform of the voltage on it (V_P) is symmetric in the positive- and negative-V_P cases thanks to the constant capacitance, as illustrated in Fig. 2. Due to the flipping loss, V_P cannot reach V_{REC} immediately after the flipping but will be built up slowly by the intrinsic current source. Apparently, a higher V_{REC} results in a longer build-up time. When V_P is lower than V_{REC}, this period, namely, the cut-off period of FBR (T_{CO}), is found to correlate with the power output (P_{OUT}). Denoting the cut-off duty cycle as

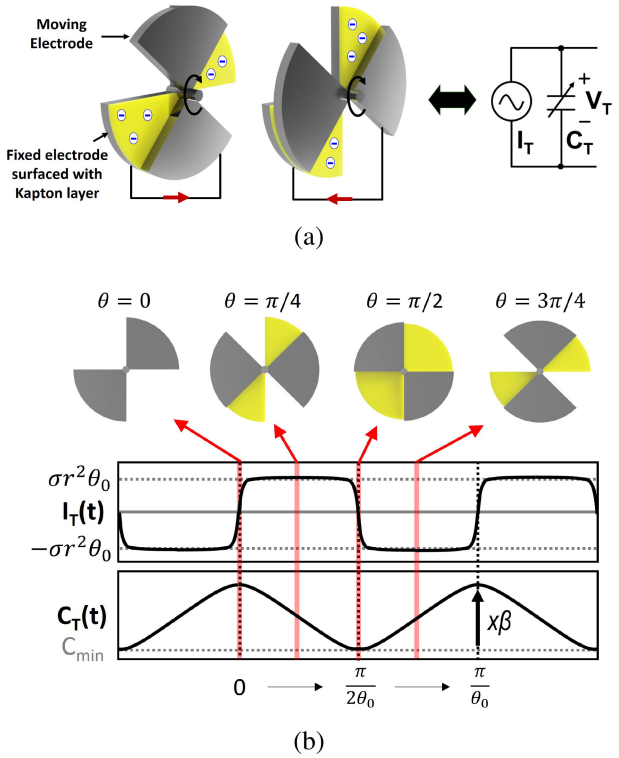

FIGURE 3. (a) Structure and model of an RS-TENG. (b) Illustrated waveform of an RS-TENG.

$D_{CO} = T_{CO}/(T_{op}/2)$, where T_{op} represents the operational period of the transducer, the mathematic correlation between D_{CO} and the MPPT efficiency (η_{MPPT}), i.e., the normalized P_{OUT} with respect to the maximum power output P_{MPP}, is given as [28]

$$\eta_{\text{MPPT}}(D_{CO}) = \frac{P_{\text{OUT}}}{P_{\text{MPP}}} = 1 - cos^2(\pi D_{CO}). \tag{1}$$

In this case, the MPP can be easily tracked by detecting the D_{CO} of a bias-flip rectifier. Compared to other MPPT techniques, the DCB MPPT eliminates the need to measure the V_{OC} or the current output, making it suitable to be applied to TEH.

B. TENG OUTPUT UNDER BIAS-FLIP RECTIFIER

Different from PT, TENG has asymmetric output in positive- and negative-I_T phases, so the relationship between its η_{MPPT} and D_{CO} becomes very different from that in piezoelectric energy harvesting. Besides, they have a distinct mechanical operation, which also affects the optimum D_{CO} at MPP ($D_{CO,mpp}$).

To test and validate the proposed rectifier and MPPT to be presented later, a rotational-sliding TENG (RS-TENG) is fabricated in-house, which is advantageous in harvesting energy from rotational mechanical movement with a small form factor and long-term stability. A model of RS-TENG is illustrated in Fig. 3(a), which contains a fixed electrode surfaced by a Kapton layer and a moving electrode coated with gold. Either electrode consists of two 90° connected metal sectors. During the operation, the triboelectric charge is generated from the friction between the Kapton layer and the moving electrode, which induces electrostatic potential between the electrodes. As a result, RS-TENG outputs alternating current, and the electrodes generate a time-varying capacitor between them.

The fundamental expression of I_T and C_T can be written as follows:

$$I_T = \frac{d}{dt}(\sigma S(t)) \tag{2}$$

$$C_T = \frac{\epsilon_0 S(t)}{d_{\text{air}} + d_{\text{Kapton}}/\epsilon_r} \tag{3}$$

where σ represents triboelectric charge density on the Kapton layer, $S(t)$ is the time-dependent overlapping area between electrodes, ϵ_0 denotes the vacuum permittivity, d_{air} and d_{Kapton} represent the width of the air gap and thickness of the Kapton layer, respectively, and ϵ_r represents the relative permittivity of the Kapton material.

Denoting that the RS-TENG is operating under a constant angular velocity θ_0, I_T turns out to be a constant value independent from the time, while C_T shows a first-order relationship with respect to time. Their representative waveforms are presented in Fig. 3(b) and their approximated expressions are shown in the following equations:

$$\text{Case 1: } 0 \le t < \frac{\pi}{2\theta_0} \quad \begin{matrix} I_T \approx \sigma r^2\theta_0 \\ C_T \approx \left(\frac{2}{\pi}(1-\beta)\theta_0 t + \beta\right) C_{\text{min}} \end{matrix} \tag{4}$$

$$\text{Case 2: } \frac{\pi}{2\theta_0} \le t < \frac{\pi}{\theta_0} \quad \begin{matrix} I_T \approx -\sigma r^2\theta_0 \\ C_T \approx \left(\frac{2}{\pi}(\beta-1)\theta_0 t + 1\right) C_{\text{min}} \end{matrix} \tag{5}$$

where r corresponds to the radius of the sector, and β represents the capacitance varying ratio ($\beta = C_{\text{max}}/C_{\text{min}}$). Due to the symmetry in the electrodes, we only need to analyze the performance in one cycle, which corresponds to a rotation angle range of $[0, \pi/2)$.

Then, the output of the RS-TENG, when applied to a bias-flip rectifier, can be analyzed. Fig. 4 illustrates the waveforms of the voltage on an RS-TENG (V_T) in two situations. Due to the varying capacitance, we achieve two cut-off periods in the positive- and negative-I_T semi-period with V_T lower than V_{REC}, i.e., $T_{CO,p}$ and $T_{CO,n}$, respectively. Both of them are monotonically increasing with the increase of V_{REC}. However, when V_{REC} arrives at a certain value, the rectifier is completely cut off in the negative-I_T semi-period due to the increasing C_T, resulting in a constant $T_{CO,n}$ equal to half of the cycle as shown in Fig. 4. If the MPP occurs in this case, the MPPT based on $T_{CO,n}$ cannot work. Therefore, we choose to use $D_{CO} = T_{CO,p}/(T_{op}/2)$ to implement the DCB MPPT for TENG.

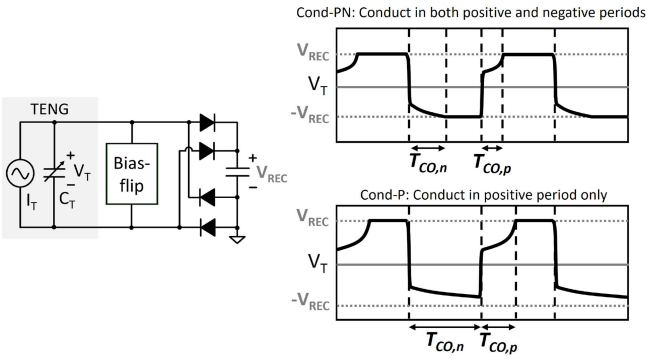

FIGURE 4. Waveform of bias-flip rectifier for TENG in different conduction conditions.

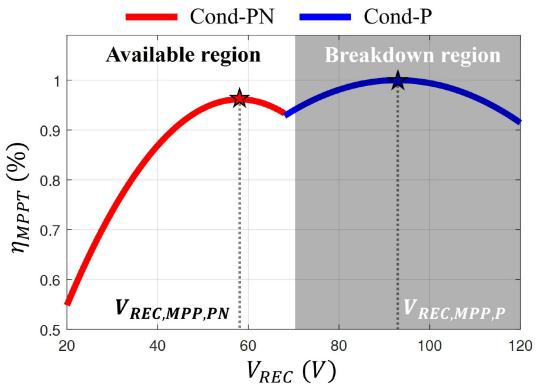

FIGURE 5. MPPT efficiency (η_{MPPT}) versus output voltage considering the system's breakdown voltage with $\eta_{F,p} = \eta_{F,n} = 30\%$ and $\beta = 2.2$.

III. THEORETICAL ANALYSIS ON THE MPP DUTY CYCLE OF TENG

As shown in Fig. 4, the rectifier can operate in two different conduction conditions based on the V_{REC} level: 1) conduction in both positive and negative periods (Cond-PN) and 2) conduction in positive period only (Cond-P). The two conditions are analyzed and combined to achieve the system's real $D_{CO,mpp}$.

A. COND-PN: THE RECTIFIER CONDUCTS IN BOTH POSITIVE- AND NEGATIVE-I_T SEMI-PERIOD

In this case, triboelectric energy is extracted in both semi-periods, which usually occurs due to the small C_T variation ratio, β, or low-voltage flipping efficiency. Therefore, the power output in Cond-PN in one cycle $E_{cycle,PN}$ can be derived as [29]

$$E_{\mathrm{cycle,PN}} = -\left[\beta\left(1-\eta_{F,n}\right)+1-\eta_{F,p}\right]C_{\min}V_{\mathrm{REC}}^2 + 2Q_{SP}V_{\mathrm{REC}}\left(\text{when } V_{\mathrm{REC}} < \frac{Q_{SP}}{(\beta-\eta_{F,p})C_{\min}}\right) \tag{6}$$

where $\eta_{F,p}$ and $\eta_{F,n}$ represent the voltage flipping efficiency when I_T switches from positive to negative and from negative to positive, respectively; Q_{SP} represents the output charge of I_T within one semi-period ($T_{op}/2$) derived from the following equation:

$$Q_{SP} = \int_0^{\frac{T_{op}}{2}} |I_T(t)|dt = \sigma r^2\theta_0\frac{T_{op}}{2}. \tag{7}$$

Substituting (7) to (6), the expression of V_{REC} when $E_{\mathrm{cycle-PN}}$ reaches the peak can be derived as

$$V_{\mathrm{REC,MPP,PN}} = \frac{\sigma r^2\theta_0 T_{op}}{2\left[\beta\left(1-\eta_{F,n}\right)+1-\eta_{F,p}\right]C_{\min}}. \tag{8}$$

Since the RS-TENG is open during $T_{CO,p}$, the expression of V_T with regard to time during $T_{CO,p}$ can be derived as

$$V_{T,PN}(t) = \frac{\beta\eta_{F,n}C_{\min}V_{\mathrm{REC}} + \sigma r^2\theta_0 t}{\left[\frac{2}{\pi}(1-\beta)\theta_0 t + \beta\right]C_{\min}}. \tag{9}$$

As $V_{T,PN}$ reaches V_{REC} at $t = T_{CO,p}$, we could derive the relationship between V_{REC} and the current $T_{CO,p}$ as follows:

$$V_{\mathrm{REC,PN}} = \frac{\sigma r^2\theta_0 T_{CO,p}}{\left[\beta\left(1-\eta_{F,n}\right)+\frac{2}{\pi}(1-\beta)\theta_0 T_{CO,p}\right]C_{\min}}. \tag{10}$$

Denote D_{CO} as

$$D_{\mathrm{CO}} = \frac{T_{\mathrm{CO},p}}{T_{op}/2} = \frac{2\theta_0}{\pi}T_{\mathrm{CO},p}. \tag{11}$$

Given that the interface is operating at the MPP, i.e., $V_{REC,PN} = V_{REC,MPP,PN}$, (8) can be substituted to (10), and then the expression of D_{CO} at MPP in Cond-PN, $D_{CO,MPP,PN}$, can be derived as

$$D_{\mathrm{CO,MPP,PN}} = \frac{\beta\left(1-\eta_{F,n}\right)}{2\beta-\beta\eta_{F,n}-\eta_{F,p}}. \tag{12}$$

B. COND-P: THE RECTIFIER ONLY CONDUCTS IN THE POSITIVE-I_T SEMI-PERIOD

In Cond-P, V_T can never reach V_{REC} in the negative-I_T semi-period possibly due to the high β or high flipping efficiency. Thus, the triboelectric energy is only harvested in the positive semi-period, and the energy harvested in one cycle could be derived as [29]

$$E_{\mathrm{cycle},P} = -\left(1-\eta_{F,p}\eta_{F,n}\right)C_{\min}V_{\mathrm{REC}}^2 + \left(1+\eta_{F,n}\right)Q_{SP}V_{\mathrm{REC}} \left(\text{when } V_{\mathrm{REC}} \geq \frac{Q_{SP}}{(\beta-\eta_{F,p})C_{\min}}\right). \tag{13}$$

Then, the expression of $V_{\mathrm{REC,MPP}}$ in this condition can be derived as

$$V_{\mathrm{REC,MPP},P} = \frac{\left(1+\eta_{F,n}\right)\sigma r^2\theta_0 T_{op}}{4\left(1-\eta_{F,p}\eta_{F,n}\right)C_{\min}}. \tag{14}$$

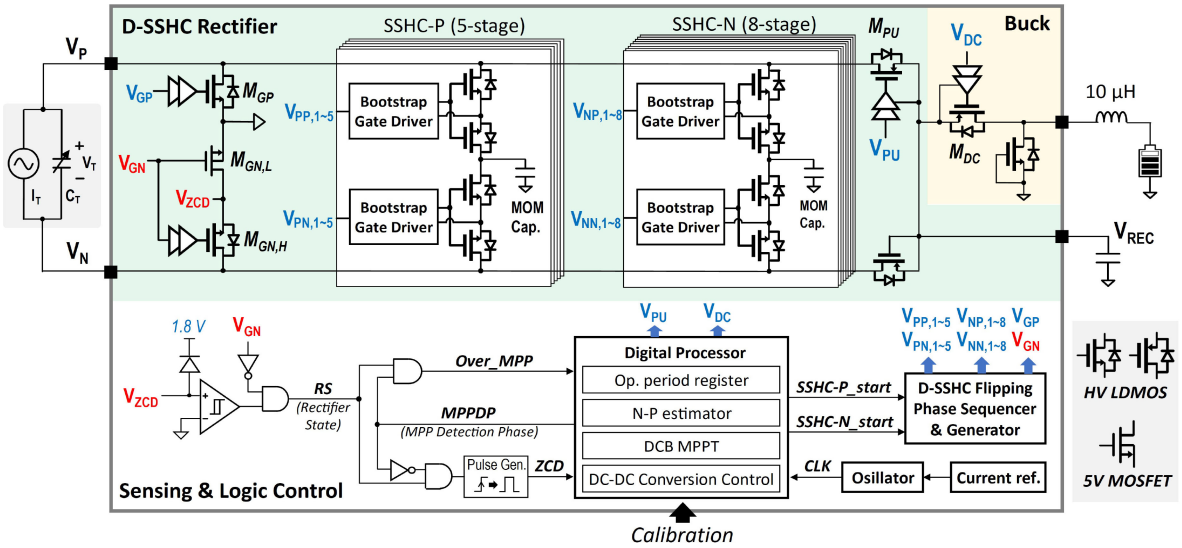

FIGURE 6. System architecture of the proposed rectifier.

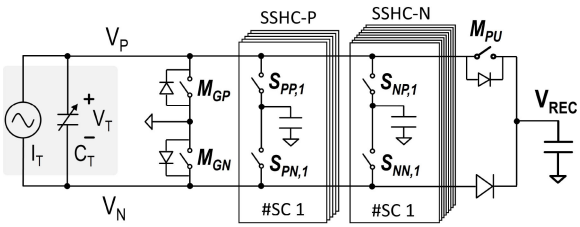

FIGURE 7. Simplified schematic of the power stage of the D-SSHC rectifier.

And the expression of V_T with regard to time during $T_{CO,p}$ can be derived as

$$V_{T,P}(t) = \frac{\eta_{F,n}\left(\eta_{F,p}C_{\min}V_{\mathrm{REC}} + Q_{SP}\right) + \sigma r^2\theta_0 t}{\left[\frac{2}{\pi}(1-\beta)\theta_0 t + \beta\right]C_{\min}}. \quad (15)$$

After substituting $t = T_{\mathrm{CO},p}$ and $V_{\mathrm{REC}} = V_{\mathrm{REC,MPP},P}$ to (15), $D_{\mathrm{CO,MPP}}$ in Cond-P becomes

$$D_{\mathrm{CO,MPP},P} = \frac{\beta\left(1-\eta_{F,n}\right) - \eta_{F,n}\left(2+\eta_{F,p}-\eta_{F,p}\eta_{F,n}\right)}{\beta\left(1+\eta_{F,n}\right) + 1 - \eta_{F,n} - 2\eta_{F,p}\eta_{F,n}}. \quad (16)$$

C. REAL $D_{CO,MPP}$ OF TENG

According to (12) and (16), the optimal D_{CO} corresponding to MPPs in Cond-PN and Cond-P differs. A simple way to find the systematic MPP is to compare the E_{cycle} in both conditions and select the higher one and its corresponding $D_{\mathrm{CO,MPP}}$ as the target optimum D_{CO}. By substituting (8) to (6) and (14) to (13), the theoretical maximum power output in both conditions can be derived, respectively, as

$$E_{\mathrm{cycle,MPP,PN}} = \frac{1}{1-\eta_{F,p}+\beta\left(1-\eta_{F,n}\right)}\frac{Q_{SP}^2}{C_{\min}} \quad (17)$$

$$E_{\mathrm{cycle,MPP},P} = \frac{\left(1+\eta_{F,n}\right)^2}{4\left(1-\eta_{F,p}\eta_{F,p}\right)}\frac{Q_{SP}^2}{C_{\min}} \quad (18)$$

Hereby, if $E_{cycle,MPP,PN}$ is greater than $E_{\mathrm{cycle,MPP},P}$, $D_{\mathrm{CO,MPP}}$ should be equal to $D_{\mathrm{CO,MPP,PN}}$; otherwise, $D_{CO,MPP,P}$. However, an exception is presented in Fig. 5. The Cond-PN and Cond-P curves are derived from the ratios of $E_{\mathrm{cycle,PN}}$ (6) to $E_{\mathrm{cycle,MPP,PN}}$, and $E_{\mathrm{cycle},P}$ (13) to $E_{\mathrm{cycle,MPP},P}$, respectively. This plot of η_{MPPT} versus V_{REC} in a certain situation shows a power output valley between $V_{\mathrm{REC,MPP,PN}}$ and $V_{\mathrm{REC,MPP},P}$. If the technical voltage of the chip is located within this valley, V_{REC} can never reach $V_{\mathrm{REC,MPP},P}$, and the practical MPP should be $E_{\mathrm{cycle,MPP,PN}}$ despite that $E_{\mathrm{cycle,MPP,PN}} < E_{\mathrm{cycle,MPP},P}$. Therefore, if $V_{\mathrm{REC,MPP},P}$ is greater than the technical voltage, the energy output at the maximum V_{REC} should also be considered.

Furthermore, $D_{\mathrm{CO,MPP}}$ in the context of TEH is theoretically determined by β, $\eta_{F,p}$, and $\eta_{F,n}$, which are somewhat dependent on the features of the transducers and rectifiers. However, it is worth noting that, in many practical scenarios, e.g., the combination of RS-TENG and the proposed bias-flip rectifier presented in this work, the β and flipping efficiencies remain constant. From the perspective of long-term stability, the major aging factor for the RS-TENG is the wear and tear of the Kapton layer, which leads to a reduction of d_{Kapton} in (3). However, variations in electrode spacing, whether due to aging or other factors, do not affect β since it is the fraction of $C_{\max}$ and $C_{\min}$, which is solely determined by the overlapping area between electrodes. Moreover, since d_{Kapton} is typically 2–4 times smaller than d_{air}, and when accounting for its permittivity, the effective contribution of the Kapton layer is even smaller—resulting in less than 10% variation in total capacitance due to wear. In this case, the flipping efficiencies, which depend on both the TENG capacitance and the flipping capacitance of the D-SSHC rectifier, also barely vary. This ensures stable $D_{\mathrm{CO,MPP}}$ and

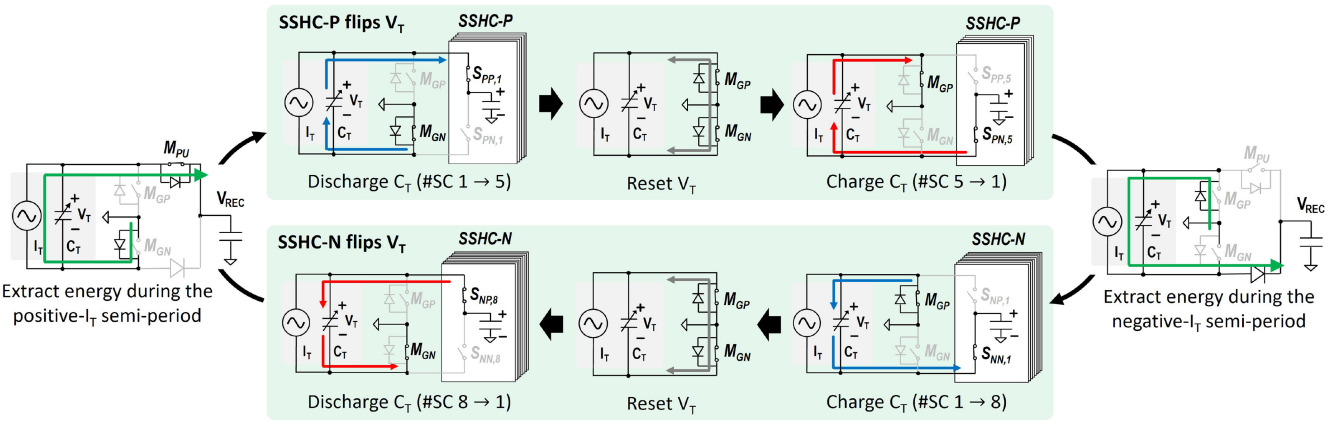

FIGURE 8. Operational phases of the D-SSHC rectifier.

sustained MPPT efficiency over prolonged operation. Under such conditions, a one-time trimming would be sufficient to enable the TEH system to operate at or near its optimal point over an extended period.

IV. SYSTEM IMPLEMENTATION

Fig. 6 presents the top architecture of the proposed system, which is mainly composed of three blocks: 1) a dual-SSHC (D-SSHC) rectifier; 2) a buck converter; and 3) a sensing and logic controller. Details are introduced in the following sections.

A. D-SSHC RECTIFIER

For the SSHC technique, its flipping efficiency becomes stable when the voltage on each flipping capacitor is settled, i.e., the voltage across the flipping capacitor before and after the flipping is the same. In piezoelectric energy harvesting, due to the constant capacitance in the PT, one SSHC block is enough to flip the voltage in both directions. However, in TEH, V_T voltage levels at different flipping moments differ due to the varying C_T, e.g., as described in the Cond-P in Section III-B. In this case, sharing one SSHC block for every flipping moment will lead to significant degradation in the flipping efficiency.

Consequently, two switched-capacitor banks (SSHC-P and SSHC-N) are employed in the proposed TEH interface to flip V_T to accommodate both flipping polarities for optimal flip efficiency. The switched capacitors are implemented with on-chip metal-oxide-metal capacitors (MOMCAPs) controlled by laterally diffused MOSFET (LDMOS) switches. Each switch consists of two LDMOS transistors with their source terminals connected together to avoid latch-up through their body diodes. In addition to the switched capacitors, the D-SSHC rectifier also includes an FBR with active switches (M_{GP}, $M_{GN,L}$, $M_{GN,H}$, and M_{PU}) to extract energy.

To show the operational principle of the D-SSHC rectifier clearly, a simplified schematic of the proposed D-SSHC rectifier is presented in Fig. 7, with MOSFETs replaced by switch symbols. The detailed operational phases of the D-SSHC rectifier are shown in Fig. 8. During most operation

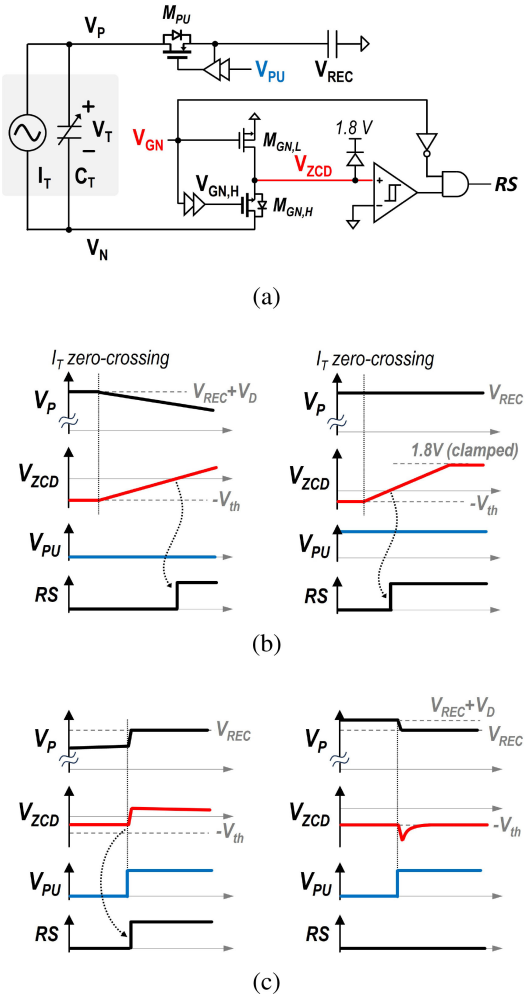

FIGURE 9. RSS. (a) Circuit diagram. (b) Waveforms around the positive flipping moment when M_{PU} is turned off and turned on, respectively. (c) Waveforms when actively checking the rectifier state while the rectifier is conducting and cut-off, respectively.

times, the SSHC blocks are disabled, while the FBR extracts energy by utilizing the body diodes of the LDMOS and 5-V MOSFET in M_{GP}, M_{GN}, and M_{PU}. The forward voltage

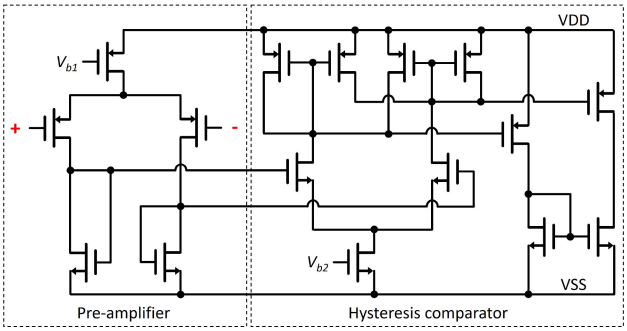

FIGURE 10. Hysteresis comparator with a preamplifier used in RSS.

drop on the body diodes is typically around 600 mV, which is much lower than the extracted voltage V_{REC}; thus the loss on the diodes is negligible. M_{PU} is turned on at a certain moment to sense the rectifier state, which will be elucidated in the following section. When the positive flipping moment (V_T is positive, C_T is minimum, and I_T crosses zero) reaches, a 5-stage SSHC-P block is enabled to flip V_T, while an 8-stage SSHC-N block is enabled to flip V_T at the negative flipping moment (V_T is negative, C_T is maximum, and I_T crosses zero). More stages and larger flipping capacitance are used in SSHC-N due to the larger C_T at the negative flip moment. Due to the limited chip area, the flipping capacitance in each SSHC-P cell is 10 pF while that in each SSHC-N cell is 25 pF. Besides, different from the conventional SSHC rectifiers, which use flying capacitors, this D-SSHC rectifier always grounds one node of the flipping MOMCAPs to reduce the number of high-voltage switches and gate drivers, and eliminate the effect of plate parasitic capacitance. To build the current loop and eliminate the passive diode loss, M_{GP} and M_{GN} are turned on synchronously during the flipping operation to ground one side of the TENG.

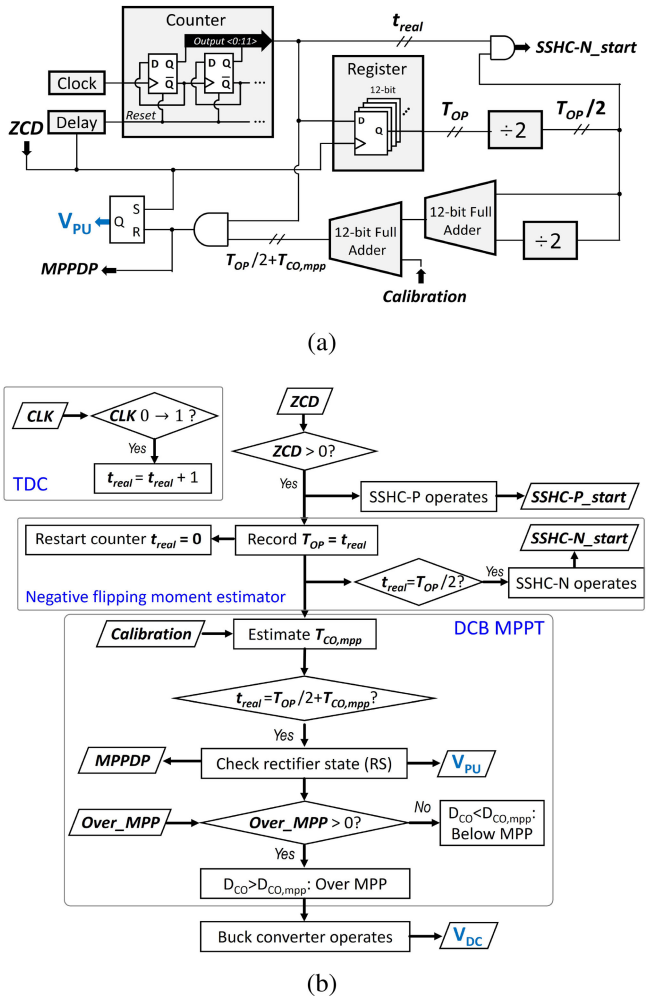

FIGURE 11. (a) Block diagram of the digital implementation and (b) workflow of the digital-DCB MPPT algorithm.

B. RECTIFIER STATE SENSING

To track the real D_{CO} and apply DCB MPPT to the TENG, detecting the state of the TENG is necessary. In this work, a rectifier state sensor (RSS) is utilized as shown in Fig. 9(a). When the TENG's state is not tracked, M_{PU} and $M_{GN,L}$ perform as passive diodes as V_{PU} and V_{GN} are at low level, while $V_{GN,H}$ is equal to 1.8 V to partially turn on $M_{GN,H}$. In this way, when $V_N < 1.8$ V, V_{ZCD} copies V_N; otherwise, $V_{ZCD} = 1.8$ V so that the low-voltage comparator and logic gates are protected. Fig. 9(b) left illustrates the waveforms of the significant signal in RSS when TENG comes to the positive flipping moment. The decrease of V_T changes the state of the rectifier from conducting to cut-off, and meanwhile, V_P decreases while V_N increases. When V_N crosses 0 V, the signal RS switches from low to high, indicating the detected positive flipping moment. In this way, V_N increases slowly since V_P decreases in the meantime, leading to a long delay between the real I_T-crossing-zero moment and the flipping moment. To fasten the detection, one way is to turn on M_{PU} so that V_P is pulled up and the decrease of V_T will be completely reflected in the increase of V_N as shown in Fig. 9(b) right. In that case, the delay of detection is improved by approximately 50%. Additionally, RSS can be used to actively detect whether the rectifier is cut-off or conducting, as shown in Fig. 9(c). The detection is implemented by pulling up V_P and then checking the voltage level of V_{ZCD}. If the rectifier is cut-off, V_T is lower than V_{REC} so after V_P is pulled up, V_{ZCD} is usually higher than 0 V, which can be sensed by RSS. On the other hand, when the rectifier is conducting, turning on M_{PU} eliminates the forward voltage drop on it and thus, will decrease V_P from $V_{\mathrm{REC}} + V_D$ to V_{REC}, where V_D represents the forward voltage drop on a passive diode. This results in a voltage drop on V_{ZCD} which will recover soon, and RS will stay low as V_{ZCD} is always lower than 0 V. In this way, the state of the rectifier is sensed actively, which assists in measuring T_{CO} and tracking the MPP of TENG. Last but not least, since RSS is sensitive to voltage signal and V_{ZCD} varies in a wide range, the comparator in RSS employs a preamplifier

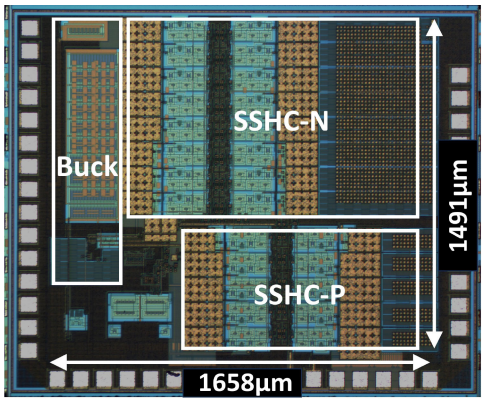

FIGURE 12. Chip micrograph.

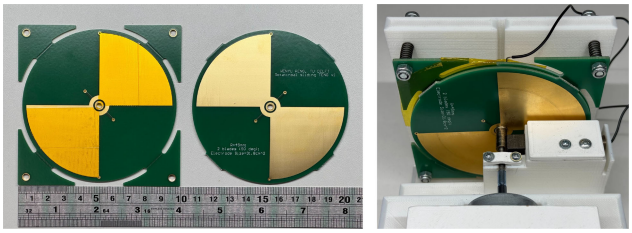

FIGURE 13. In-house fabricated RS-TENG prototype.

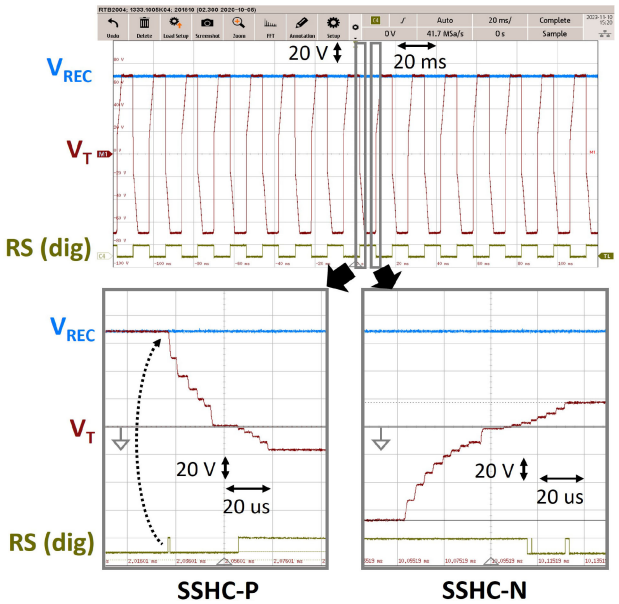

FIGURE 14. Measured waveform in a number of periods and the zoomed-in figures showing the voltage flipping moments 69 V.

with pMOS input pair to achieve high input impedance and a wide input range, whose schematic is presented in Fig. 10.

C. PHASE LOGIC AND DIGITAL DCB MPPT

The phase logic of the proposed interface, including the digital DCB MPPT processing, is processed by the digital processor block, whose simplified block diagram is shown in Fig. 11(a) while the workflow is presented in Fig. 11(b). Thanks to the proposed RSS, the positive flipping moment

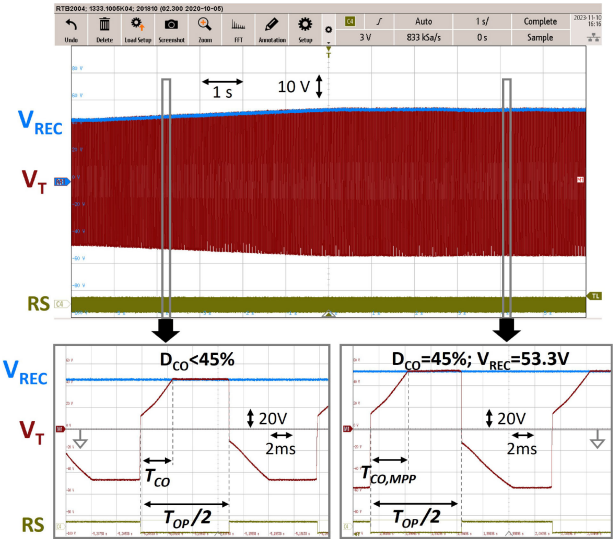

FIGURE 15. Measured waveform when tracking the MPP.

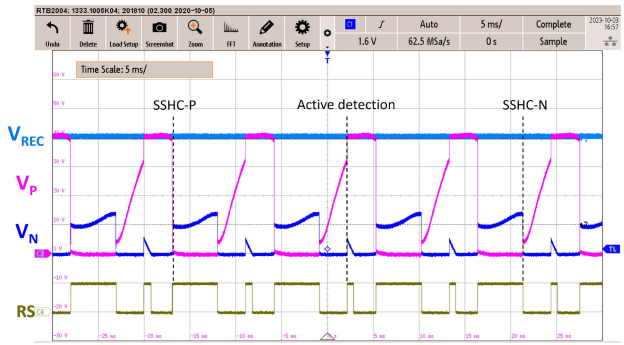

FIGURE 16. Measured waveform when D_{CO} exceeds $D_{CO,MPP}$. In this measurement, the buck converter is disabled to deactivate the MPPT.

could be detected accurately so that the SSHC-P can operate at the right time. Regarding the negative flipping moment, since the rectifier may not conduct during the negative-I_T semi-period, there could be no rectifier state switching at the negative flipping moment; therefore, the negative flipping moment is estimated by the digital processor according to the operational period (T_{op}) of the TENG. Assisted by the clock signal from a current-starving oscillator operating at 20 kHz, the counter in the digital processor digitizes the time (t_{real}). When the positive flipping moment is detected, the signal ZCD goes high, triggering the digital processor to record the current t_{real} and then reset t_{real}. After two periods, the time interval between two adjacent positive flipping moments, i.e., the period T_{op}, is achieved. Afterward, the negative flipping moment can be estimated to be coming in $T_{op}/2$ after the recent positive flipping moment, and the SSHC-N block will be operating then.

After measuring T_{op}, the digital processor could derive $T_{\text{CO,MPP}}$ according to the calculated $D_{\text{CO,MPP}}$. As aforementioned, the trackable $D_{\text{CO,MPP}}$ is normally within the range of 0.4–0.7 so the digital processor will first set $D_{\text{CO,MPP}} = 0.5$ as the default value, i.e., $T_{\text{CO,MPP}} = T_{op}/4$. After

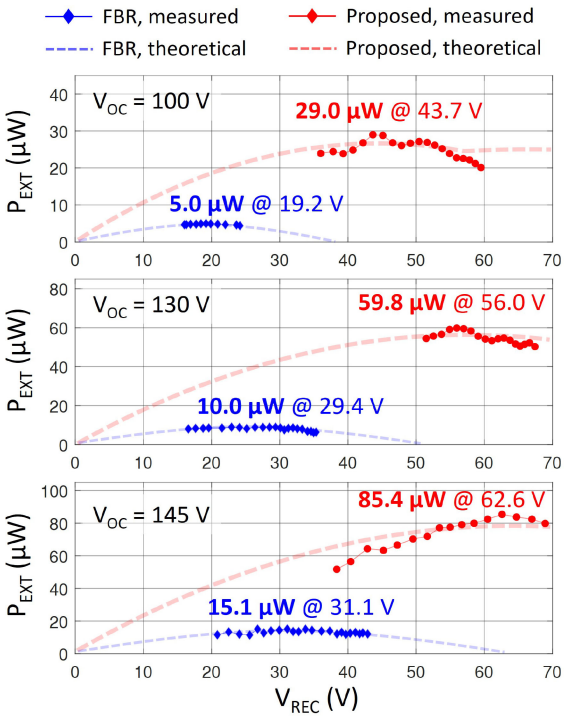

FIGURE 17. Theoretical and measured extracted energy (P_{EXT}) versus the rectification voltage (V_{REC}) under different V_{OC} when $\beta = 2$ and $f_{op} = 1/T_{op} = 70$ Hz.

TABLE 1. Measured performance of the proposed interface with three different V_{OC} values.

V_{OC}	$P_{EXT,MAX}$	$V_{REC,MPP}$	η_{MPPT}	FoM*
100 V	29.0 µW	43.7 V	93.7%	585%
130 V	59.8 µW	56.0 V	99.0%	598%
145 V	85.4 µW	62.6 V	96.0%	562%

* Figure of Merit (FoM) corresponds to the enhancement of the power output of the proposed harvester compared to that of a passive FBR.

the calibration based on the observed flipping efficiency, the real $T_{CO,MPP}$ is set. Then, the digital processor will request RSS to actively check the state of the rectifier when $t_{real} = T_{op}/2 + T_{CO,MPP}$. At this moment, if the rectifier is conducting, it means the current T_{CO} is lower than the expected $T_{CO,MPP}$ and V_{REC} has not reached the MPP. In this case, the buck converter will not work so that V_{REC} can be continuously charged to a higher level. Otherwise, if the rectifier is cut off at the detection, the signal *Over_MPP* goes high, revealing that V_{REC} has exceeded the MPP point and should be decreased; therefore, the buck converter operates. In this process, since the digital processor only operates simple recording and calculations under very low frequency (20 kHz) and supply voltage (1.4 V), the power consumption of the digital processor is quite low. The detailed power consumption is illustrated in the following section.

V. MEASUREMENT RESULTS

The proposed TEH interface is implemented in a 180-nm BCD process. Fig. 12 presents the micrograph of the chip, with an active area of 2.47 mm^2. The RS-TENG prototype

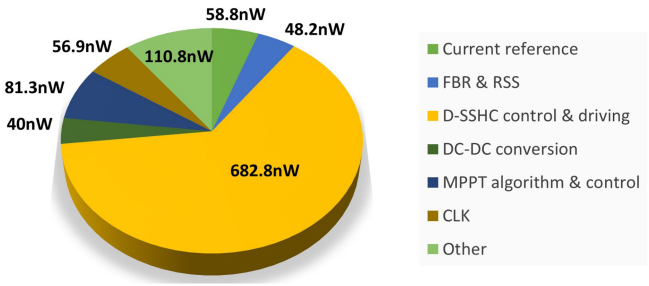

FIGURE 18. Simulated power breakdown of blocks in the proposed system.

used in the experiment is presented in Fig. 13. The disks have a radius of 45 mm and contain one electrode composed of two symmetrically aligned sectors. The measured maximum C_T of this prototype is 140 pF and the minimum value is 70 pF; therefore a capacitance varying ratio of $\beta = 2$ is employed in the DCB MPPT algorithm.

Thanks to the high-voltage tolerance of LDMOS devices and the MOMCAPs, the system is fully on-chip integrated and can efficiently extract energy from a TENG at a maximal output voltage of 70 V. Fig. 14 shows that the interface works well when $V_{REC} = 69$ V, which can occur when the MPP of a TENG exceeds 70 V. The rising edge of the RS signal triggers voltage flipping at the positive flipping moment, and the negative flipping moment is precisely estimated from period measurement. Thanks to the proposed RSS, the positive flipping moment is precisely detected when V_T only drops for around V_{TH}. Besides, the flipping process is fast, with the positive flipping taking around 40 µs and the negative flipping taking 70 µs thanks to the small C_T. Due to the limited area on the chip, the flipping capacitors have relatively small capacitance, resulting in a flipping efficiency of around 25% in both situations.

The process of MPPT is illustrated in Fig. 15. Based on the measured β and flipping efficiency, $D_{CO,MPP}$ is calculated at 45%. When the cut-off duty cycle is lower than the theoretical $D_{CO,MPP}$, the interface disables the buck converter and lets V_{REC} increase with harvested energy. When T_{CO} reaches $T_{CO,MPP}$, the MPP arrives with the current V_{REC} equal to 53.3 V. Then, the buck converter operates to regulate T_{CO} at 45% to achieve the optimum triboelectric energy extraction.

Fig. 16 presents how RSS performs when D_{CO} exceeds $D_{CO,MPP}$. In this situation, when V_P is pulled up at $T_{CO,MPP}$, the rectifier is cut off, and thus, V_N will increase, which is precisely detected as the signal RS shows. This waveform also shows the situation that V_T, the voltage difference between V_P and V_N, could differ before SSHC-P and SSHC-N. Hence, employing two separate SSHC blocks for flipping at either moment can ensure better flipping efficiency in this case.

The robustness of the digital DCB MPPT in TEH was demonstrated. During the experiment setup, we first press the rotating disk in the RS-TENG onto the fixed disk. The friction between two disks will generate a static charge

TABLE 2. Comparison table of the state of the arts.

	JSSC'20 [9]	JSSC'21 [10]	TCAS-I'21 [16]	JSSC'22 [17]		JSSC'24 [25]	**This work**
Process	0.18-μm BCD	0.18-μm BCD	0.18-μm BCD	0.18-μm BCD		0.18-μm BCD	**0.18-μm BCD**
Transducer	TENG	TENG	TENG	TENG		TENG	**TENG**
Inherent Capacitance	Varying	Varying	Varying	Constant		Varying	**Varying**
Energy Extraction Methods	Dual-Output FBR	Dual-Output FBR	P-SSHI	MCS-BF		ECB	**D-SSHC**
Fully Integrated Rectifier	Yes	Yes	No	No		Yes	**Yes**
Bias-Flip employed	No	No	Yes	Yes		Yes	**Yes**
Bias-Flip Type	N/A	N/A	Inductor-based	Inductor-based		Capacitor-based	**Capacitor-based**
DC-DC Conversion	Dual-Input Buck	Dual-Input Buck	Buck+SC	Reconfigurable SC		Buck	**Buck**
Inductance	1 mH	10 mH	1 mH	10 mH		10 μH	**10 μH**
MPPT Employed	Yes	Yes	No	No		Conditional ($\beta > 6$)	**Yes**
MPPT Method	FOCV	FOCV	N/A	N/A		Auto-MPPT @ 70V	**Digital DCB**
MPPT Efficiency	97%	89.7%	N/A	N/A		99%	**99%**
Max. Input Voltage (V)	70	70	70	130 (2-chip)	195 (3-chip)	70	**70**
Extracted Power (μW)	4.5 – 16	3.9 – 10.5	722	1211	823	127.6	**85.4**
Max. P_{EXT}/P_{FBR}	N/A	N/A	1.62	3.14	2.14	14.0	**5.98**

on the Kapton layer. Then, we recover the gap between the disks to avoid the interruption from the friction. The parameters needed in the DCB MPPT (β and the flipping efficiency) are measured under this condition. In this case, the static charge will gradually diminish as time passes, resulting in a decrease in the V_{OC} of TENG while other parameters are constant. In this way, the insensitivity of the DCB MPPT to V_{OC} can be demonstrated. Fig. 17 shows the energy extracted by the D-SSHC rectifier when $\beta = 2$ and the operational frequency is 70 Hz while V_{OC} is varying. The maximum extracted power (P_{EXT}) is achieved at 85.4 µW when V_{REC} =62.6 V. The maximum power output and the MPPT efficiency (η_{MPPT}) under each situation are presented in Table 1. Due to the inevitable time dependence of V_{OC}, the measured power output deviates from the theoretical constant-V_{OC} condition, leading to minor variations in MPPT efficiency. It is shown that in all three situations, η_{MPPT} is higher than 93%, with the peak η_{MPPT} among them reaching 99% when V_{OC} =130 V. This shows good robustness of the DCB MPPT in TEH and also verifies the effectiveness of the theoretical $D_{\mathrm{CO,MPP}}$ expression. Meanwhile, the interface achieves an energy extraction improvement of 598% at the maximum compared to an FBR implemented with the same BCD process with the proposed rectifier.

The simulated power breakdown of key blocks is presented in Fig. 18. The overall power consumption is 1078 nW, which consumes less than 2% of the harvested energy. A significant amount of power (682.8 nW) is consumed to control and drive the D-SSHC power stages due to the high voltage and parasitic capacitance of the LDMOS switches. Since most blocks are designed with 1.8-V MOSFET and driven by 1.4 V, the power consumption of each of the remaining blocks is suppressed to lower than 100 nW, making the system self-sustained and practical in IoT application scenarios.

Table 2 compares this work with state-of-the-art designs. This chip was evaluated with an RS-TENG to show its MPPT and energy extraction performance. However, the proposed D-SSHC rectifier combined with the DCB MPPT algorithm offers broad applicability and robustness. It can effectively track the MPP across various TENG architectures and a wide range of operating conditions, including cases where the capacitance variation is moderate or the system is subject to mechanical wear. This generality makes the proposed approach well suited for real-world deployment in diverse TENG-based systems. Furthermore, the proposed system achieves a small form factor by employing a few off-chip components, including a 10-μH inductor and a 0805-package 1-μF capacitor. Last but not least, this work is the first to employ a digital DCB-MPPT technique in TEH, achieving up to 99% MPPT efficiency, as defined by the ratio of the power extracted by the MPPT algorithm to the actual peak output power across the full V_{REC} range. Advantageous in continuous MPPT without much interruption to the energy source, the proposed rectifier achieves high MPPT efficiency and energy extraction improvement not requiring the TENG to have a higher capacitance varying ratio.

VI. CONCLUSION

This article presents a TEH interface employing a fully integrated D-SSHC rectifier and digital DCB MPPT algorithm. The proposed rectifier achieves miniaturization and improves the flipping efficiency when facing the asymmetric output of TENG caused by the varying intrinsic capacitance. This article elucidates the theoretical analysis of the DCB MPPT for such a TENG. With the obtained theoretical $D_{\mathrm{CO,MPP}}$, the MPP of a TENG can be easily tracked, leading to high MPPT efficiency and improved energy extraction performance. This chip was designed and fabricated with 0.18-μm BCD process with a technical voltage of 70 V. According to the measurement results, it achieves a maximum 99% MPPT efficiency and 5.98 times improvement in energy extraction compared to a conventional FBR.

REFERENCES

[1] L. Zhou, D. Liu, J. Wang, and Z. L. Wang, "Triboelectric nanogenerators: Fundamental physics and potential applications," *Friction*, vol. 8, no. 3, pp. 481–506, 2020.

[2] J. S. Y. Tan et al., "A fully energy-autonomous temperature-to-time converter powered by a triboelectric energy harvester for biomedical applications," *IEEE J. Solid-State Circuits*, vol. 56, no. 10, pp. 2913–2923, Oct. 2021.

[3] H. Ouyang et al., "Symbiotic cardiac pacemaker," *Nat. Commun.*, vol. 10, no. 1, p. 1821, 2019.

[4] B. Huang, P. Wang, L. Wang, S. Yang, and D. Wu, "Recent advances in ocean wave energy harvesting by triboelectric nanogenerator: An overview," *Nanotechnol. Rev.*, vol. 9, no. 1, pp. 716–735, 2020.

[5] P. Bai et al., "Cylindrical rotating triboelectric nanogenerator," *ACS Nano*, vol. 7, no. 7, pp. 6361–6366, 2013.

[6] Y. Zhou, P. Zhang, J. Li, and X. Mao, "Recent progress of triboelectric nanogenerator-based power management and information processing circuit," *Mater. Today Sustainabil.*, vol. 23, Sep. 2023, Art. no. 100426.

[7] W. Peng and S. Du, "The advances in conversion techniques in triboelectric energy harvesting: A review," *IEEE Trans. Circuits Syst. I, Reg. Papers*, vol. 70, no. 7, pp. 3049–3062, Jul. 2023.

[8] I. Park, J. Maeng, D. Lim, M. Shim, J. Jeong, and C. Kim, "A 4.5-to-16μW integrated triboelectric energy-harvesting system based on high-voltage dual-input buck converter with MPPT and 70V maximum input voltage," in *Proc. IEEE Int. Solid-State Circuits Conf. (ISSCC)*, 2018, pp. 146–148.

[9] I. Park, J. Maeng, M. Shim, J. Jeong, and C. Kim, "A high-voltage dual-input buck converter achieving 52% maximum end-to-end efficiency for triboelectric energy-harvesting applications," *IEEE J. Solid-State Circuits*, vol. 55, no. 5, pp. 1324–1336, May 2020.

[10] J. Maeng, I. Park, M. Shim, J. Jeong, and C. Kim, "A high-voltage dual-input buck converter with bidirectional inductor current for triboelectric energy-harvesting applications," *IEEE J. Solid-State Circuits*, vol. 56, no. 2, pp. 541–553, Feb. 2021.

[11] Y. Su, M. Yanagisawa, and Y. Shi, "A dual-output rectifier-based self-powered interface circuit for triboelectric nanogenerators," *IEEE Trans. Power Electron.*, vol. 39, no. 6, pp. 6630–6634, Jun. 2024.

[12] S. Xu, L. Zhang, W. Ding, H. Guo, X. Wang, and Z. L. Wang, "Self-doubled-rectification of triboelectric nanogenerator," *Nano Energy*, vol. 66, 2019, Art. no. 104165.

[13] A. Ghaffarinejad et al., "A conditioning circuit with exponential enhancement of output energy for triboelectric nanogenerator," *Nano Energy*, vol. 51, pp. 173–184, Sep. 2018.

[14] H. Zhang, F. Marty, D. Galayko, N. Hodzic, and P. Basset, "High-voltage MEMS plasma switch for boosting the energy transfer efficiency in triboelectric nanogenerators," in *Proc. IEEE 33rd Int. Conf. Micro Electro Mech. Syst. (MEMS)*, 2020, pp. 610–613.

[15] Y. K. Ramadass and A. P. Chandrakasan, "An efficient piezoelectric energy harvesting interface circuit using a bias-flip rectifier and shared inductor," *IEEE J. Solid-State Circuits*, vol. 45, no. 1, pp. 189–204, Jan. 2010.

[16] I. Kara, M. Becermis, M. A.-A. Kamar, M. Aktan, H. Dogan, and S. Mutlu, "A 70-to-2 V triboelectric energy harvesting system Utilizing parallel-SSHI rectifier and DC–DC converters," *IEEE Trans. Circuits Syst. I, Reg. Papers*, vol. 68, no. 1, pp. 210–223, Jan. 2021.

[17] J. Lee, S.-H. Lee, G.-G. Kang, J.-H. Kim, G.-H. Cho, and H.-S. Kim, "A triboelectric energy-harvesting interface with scalable multi-chip-stacked bias-flip and daisy-chained synchronous signaling techniques," *IEEE J. Solid-State Circuits*, vol. 57, no. 12, pp. 3825–3839, Dec. 2022.

[18] M. Pathak, S. Xie, C. Huang, and R. Kumar, "High-voltage triboelectric energy harvesting using multi-shot energy extraction in 70-V BCD process," *IEEE Trans. Circuits Syst. II, Exp. Briefs*, vol. 69, no. 5, pp. 2513–2517, May 2022.

[19] S. Du and A. A. Seshia, "An inductorless bias-flip rectifier for piezoelectric energy harvesting," *IEEE J. Solid-State Circuits*, vol. 52, no. 10, pp. 2746–2757, Oct. 2017.

[20] W. Peng, X. Yue, W. van Driel, G. Zhang, and S. Du, "A 70-V fully integrated dual-SSHC rectifier for triboelectric energy harvesting with full-digital duty-cycle-based MPPT achieving 5% power extraction enhancement," in *Proc. IEEE Custom Integr. Circuits Conf. (CICC)*, 2024, pp. 1–2.

[21] Z. Chen, M. K. Law, P. I. Mak, W. H. Ki, and R. P. Martins, "Fully integrated inductor-less flipping-capacitor rectifier for piezoelectric energy harvesting," *IEEE J. Solid-State Circuits*, vol. 52, no. 12, pp. 3168–3180, Dec. 2017.

[22] S. Du, Y. Jia, C. Zhao, G. A. J. Amaratunga, and A. A. Seshia, "A fully integrated split-electrode SSHC rectifier for piezoelectric energy harvesting," *IEEE J. Solid-State Circuits*, vol. 54, no. 6, pp. 1733–1743, Jun. 2019.

[23] Z. Chen, M. Law, P. Mak, X. Zeng, and R. P. Martins, "Piezoelectric energy-harvesting interface using split-phase flipping-capacitor rectifier with capacitor reuse for input power adaptation," *IEEE J. Solid-State Circuits*, vol. 55, no. 8, pp. 2106–2117, Aug. 2020.

[24] W. Peng, X. Yue, L. Pakula, and S. Du, "31.11 A capacitor-based bias-flip rectifier with electrostatic charge boosting for triboelectric energy harvesting achieving auto-MPPT at breakdown voltage and 14X power extraction improvement," in *Proc. IEEE Int. Solid-State Circuits Conf. (ISSCC)*, 2024, pp. 516–518.

[25] W. Peng, X. Yue, W. D. van Driel, G. Zhang, and S. Du, "A fully integrated electrostatic charge boosting rectifier for triboelectric energy harvesting," *IEEE J. Solid-State Circuits*, vol. 60, no. 6, pp. 2158–2169, Jun. 2025.

[26] S. Bandyopadhyay and A. P. Chandrakasan, "Platform architecture for solar, thermal, and vibration energy combining with MPPT and single inductor," *IEEE J. Solid-State Circuits*, vol. 47, no. 9, pp. 2199–2215, Sep. 2012.

[27] S. Uprety and H. Lee, "A 0.65-mW-to-1-W photovoltaic energy harvester with irradiance-aware auto-configurable hybrid MPPT achieving >95% MPPT efficiency and 2.9-ms FOCV transient time," *IEEE J. Solid-State Circuits*, vol. 56, no. 6, pp. 1827–1836, Jun. 2021.

[28] X. Yue, S. Javvaji, Z. Tang, K. A. A. Makinwa, and S. Du, "A bias-flip rectifier with duty-cycle-based MPPT for piezoelectric energy harvesting," *IEEE J. Solid-State Circuits*, vol. 59, no. 6, pp. 1771–1781, Jun. 2024.

[29] M. Pathak and R. Kumar, "Synchronous inductor switched energy extraction circuits for triboelectric nanogenerator," *IEEE Access*, vol. 9, pp. 76938–76954, 2021.

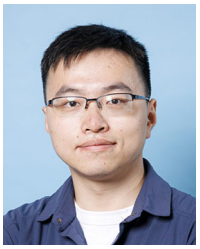

WENYU PENG (Graduate Student Member, IEEE) received the B.Sc. degree from the Glasgow College, University of Electronic Science and Technology of China, Chengdu, China, in 2020, and the M.Sc. degree from the Electronic Instrumentation Section, Department of Microelectronics, Delft University of Technology, Delft, The Netherlands, in February 2023, where he is currently pursuing the Ph.D. degree.

His current research is on triboelectric and multisource energy harvesting for wearable, biomedical, and Internet of Things autonomous sensors, including energy-efficient power management circuit designs and front-end harvester fabrications.

XINLING YUE (Graduate Student Member, IEEE) is currently pursuing the Ph.D. degree in microelectronics with the Electronic Instrumentation Laboratory, Delft University of Technology, Delft, The Netherlands.

She joined the Electronic Instrumentation Laboratory, Delft University of Technology in December 2020. Her current research interests are energy-efficient power management integrated circuits and systems, which include energy harvesting, ac/dc rectifiers, dc/dc converters, and maximum power point tracking techniques.

Ms. Yue received the Best Student Paper Award at the 2022 IEEE International Conference on Electronics Circuits and Systems, the Student Travel Grant Awards at the 2022 IEEE International Symposium on Circuits and Systems and the 2023 ISSCC, and the 2023–2024 SSCS Predoctoral Achievement Award.

WILLEM D. VAN DRIEL received the B.S. and M.S. degrees in mechanical engineering from the Eindhoven University of Technology, Eindhoven, The Netherlands, in 1992 and 1994, respectively, and the Ph.D. degree in mechanical engineering from the Delft University of Technology, Delft, The Netherlands, in 2007.

He has a >30 year track record in the reliability domain. Application areas range from healthcare, gas and oil explorations, and semiconductors. He is currently a Fellow Scientist with Signify (formerly Philips Lighting), Eindhoven. He is also a Professor with the Delft University of Technology. He has authored and co-authored more than 400 scientific publications, including journal and conference papers, book or book chapters, and invited keynote lectures. His scientific interests are solid-state lighting, microelectronics and microsystems technologies, virtual prototyping, virtual reliability qualification, and designing for reliability of microelectronics and microsystems.

Prof. van Driel is the Chair of the Organizing Committee of the IEEE Conference EuroSimE.

GUOQI ZHANG (Fellow, IEEE) received the Ph.D. degree from the Delft University of Technology, Delft, The Netherlands, in 1993.

He is a member of Netherlands Academy of Engineering, Hague, The Netherlands, and a Chair Professor for "Micro/Nanoelectronics System Integration and Reliability" with the Delft University of Technology (TUD), Delft, The Netherlands. Before joining TUD, he worked with NXP, Eindhoven, The Netherlands, and Philips, Amsterdam, The Netherlands, as a Senior Director of Technology Strategy and a Research Fellow until 2013. His research interests cover multilevel heterogeneous system integration and packaging; multiphysics and multiscale modeling and optimization of micro/nanoelectronics; digital twin and designing for reliability; wide-bandgap semiconductors sensors and components; and SSL technology.

Dr. Zhang received the IEEE Technical Field Award on packaging. He currently serves as the Secretary-General of IEEE ITRW (International Technology Roadmap of Wide Bandgap Power Semiconductors). He chaired the "More than Moore" team of European's technology platform for micro/nanoelectronics and served as the Co-Chair of the academic council of Dutch National Innovation Program on micro/nanoelectronics and embedded system. He was the founding member of MEMSLand, the NL national MEMS research consortium.

SIJUN DU (Senior Member, IEEE) received the B.Eng. degree (Hons.) in electrical engineering from the University Pierre and Marie Curie (UPMC), Paris, France, in 2011, the M.Sc. degree (Distinction) in electrical and electronic engineering from Imperial College, London, U.K., in 2012, and the Ph.D. degree in electrical engineering from the University of Cambridge, Cambridge, U.K., in January 2018.

He worked with the Laboratoire d'Informatique de Paris 6, UPMC, and then worked as an IC Engineer in Shanghai, China, from 2012 and 2014. He was a Summer Engineer Intern with Qualcomm Technology Inc., San Diego, CA, USA, in 2016. He was a Postdoctoral Researcher with the Department of Electrical Engineering and Computer Sciences, University of California at Berkeley, Berkeley, CA, USA, from 2018 to 2020. In 2020, he joined the Department of Microelectronics, Delft University of Technology, Delft, The Netherlands, as an Assistant Professor. His current research is focused on energy-efficient integrated circuits and systems, including power management integrated circuits, energy harvesting, wireless power transfer, and dc/dc converters.

Dr. Du received the Dutch Research Council (NWO) Talent Program VENI Grant in the 2021 round. He was a co-recipient of the Best Student Paper Award at IEEE ICECS 2022. He serves as an IEEE ISSCC Technical Program Committee (TPC) Member since 2025, an IEEE ISSCC Student Research Preview (SRP) Committee Member since 2023, an IEEE ICECS Subcommittee Chair in 2022 and 2024, and an IEEE ISCAS Subcommittee Chair in 2025.